Shock-Induced Instabilities on a Spherical Gas Bubble

D. Ranjan, J.H.J. Niederhaus, J.G. Oakley
M.H. Anderson, J.A. Greenough, R. Bonazza

July 2005

UWFDM-1301

Presented at the 25th International Symposium on Shock Waves (ISSW25), Bangalore, India, 17-22 July 2005, Paper 1197-2.

FUSION TECHNOLOGY INSTITUTE

UNIVERSITY OF WISCONSIN

MADISON WISCONSIN

Shock-Induced Instabilities on a Spherical Gas Bubble

D. Ranjan, J.H.J. Niederhaus, J.G. Oakley,
M.H. Anderson, J.A. Greenough, R. Bonazza

Fusion Technology Institute
University of Wisconsin
1500 Engineering Drive
Madison, WI 53706

http://fti.neep.wisc.edu

July 2005

UWFDM-1301

Presented at the 25th International Symposium on Shock Waves (ISSW25), Bangalore, India, 17-22 July 2005, Paper 1197-2.

Shock-induced instabilities on a spherical gas bubble

D. Ranjan[1], J.H.J. Niederhaus[1], J.G. Oakley[1], M.H. Anderson[1], J.A. Greenough[2], and R. Bonazza[1]

[1] *University of Wisconsin-Madison, Madison, WI, USA*
[2] *Lawrence Livermore National Laboratory, Livermore, CA, USA*

Abstract. Experiments studying the compression and unstable growth of an argon bubble in a nitrogen environment, subjected to planar shock wave ($1.32 \leq M < 4$) are performed in a vertical shock tube of square internal cross section. In parallel with laboratory experiments, a computational investigation is carried out with the multi-fluid compressible hydrodynamics code RAPTOR, using adaptive mesh refinement to achieve high resolution of the fluid interfaces. Experiments and computations confirm that the interaction of a planar shock wave propagating in nitrogen with a free-falling spherical soap bubble filled with argon first deforms the bubble into an oblate disk-like object and, subsequently, into a vortex ring. At later times, however, secondary features appear in the flow, which result from small-scale nonuniformities present in the initial condition. The evolution of the bubble is characterized, and integral length scale measurements are analyzed on a non-dimensional time scale for incident shocks within a range of Mach numbers.

1 Introduction

In any multi-component flow with non-zero pressure gradients at fluid interfaces, instabilities arise when perturbations are present, as vorticity may develop baroclinically on an interface due to the misalignment of local pressure and density gradients. These phenomena are generally known as the Rayleigh-Taylor and Richtmyer-Meshkov instabilities (RTI, RMI) depending on the pressure gradient being due to a constant or impulsive acceleration, respectively. The turbulent mixing consequent to the RTI/RMI is of importance in a number of areas, including inertial confinement fusion, where it poses a significant limitation to achieving thermonuclear ignition [1]; supersonic mixing (as in a ramjet or scramjet engine); and supernova explosions [2].

One of the greatest challenges in performing RMI experiments is the preparation of the initial interface. Meshkov [3] was the first experimenter to study a shock-wave-accelerated gas-gas interface; he used a thin nitrocellulose membrane to separate the test gases, a technique that has been commonly used in many subsequent experiments.

Innovative preparation methods have been developed to eliminate the membrane and create a continuous interface. Brouillette and Sturtevant [4] and Bonazza and Sturtevant [5] used a thin flat sliding plate in a vertical shock tube to separate two gases in a light-over-heavy configuration. Jones and Jacobs [6] used a flow technique to create a flat interface, and then oscillated their vertical shock tube side-to-side to create the initial perturbation. Due to the long contact time between gases in these methods, the interface is diffuse in nature, with a relatively large diffusion thickness.

An alternative method of forming an interface for such studies is to use a thin liquid soap film, which atomizes after shock interaction. In this way, a discontinuous interface can be created, free from effects of diffusion, while keeping the film effects to a minimum. Haas and Sturtevant [7] and, more recently, Layes *et. al.* [8] conducted experiments on spherical soap bubbles supported by a holder in a horizontal shock tube for lower Mach

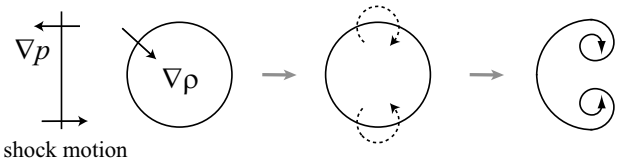

Fig. 1. 2-D cross-section of the shock-bubble interaction, for a heavy bubble in light gas.

numbers. The presence of a vortex ring structure was suggested by the shadowgraph images and inferred from the velocity measurements; however, the structure of the vortex was not completely resolved. The formation of such a vortex ring in the shock-bubble interaction is a special case of RMI. As shown in Fig. 1, baroclinic vorticity deposition by the shock wave is strongest on the diametral plane parallel to the shock wave front. shown in Fig. 1.

In the present experiments, the technique of Haas and Sturtevant is enhanced by using a retractable bubble injector and a planar imaging system. Fast retraction of the injector into a slot present in the shock tube side wall results in free flow of the bubble (which is nearly spherical) before the shock interaction, and prevents flow disruption by the holder. Planar laser imaging has been employed for flow visualization, and two shocked bubble images are captured on a single frame of the CCD array, enhancing the investigation of the evolution of the instability during a single run.

2 Experiment Description

The shock-bubble interaction is studied at different Mach numbers at the WiSTL [9]. The tube is vertical, with square internal cross section, 25×25 cm; its length is 9.2 m, with a 1.8-m-long driver section, located at the top of the tube. The shock tube facility is designed to produce a strong planar shock wave, which travels from top to bottom and interacts with experiments set up in the interface section. A soap bubble is created with a stainless steel injection system by first placing a layer of soap film on the tip of the bubble injector, and then using a pneumatic cylinder of prescribed volume to blow an argon bubble, approximately 5 cm in diameter. Prior to placing the soap film on the injector, the tube is purged of residual nitrogen, to ensure argon purity inside the bubble. The resulting argon contamination to the exterior flow is minimal (less than 1%). The soap film is estimated to be 0.5 μm thick (on average), with a slight increase in thickness at the bottom of the bubble due to gravitational flow of the soap film.

The release and free fall of the bubble are recorded at 250 fps with a CCD camera (DALSA CA-D1-0256A) and front lighting. This allows the capture of the evolution of the bubble during its release from the injector and provides an initial condition image of the bubble prior to (within 10 ms) shock interaction, during which the vorticity is deposited and the RMI initiates. The shocked bubble is imaged with a planar laser sheet produced from a Q-switched Nd:YAG laser (Continuum Surelite II). The laser beam is formed into a plane and transmitted through the center of the bottom of the shock tube. The laser is capable of two pulses separated by a minimum of 100 ns, with a pulse width of 10 ns duration. A 1024×1024 pixel array Andor (model 434) CCD camera is used to capture the Mie scattered light resulting from the laser interaction with the soap film solution (the soap film is atomized into micron sized particles during interaction with

the strong shock). The outputs from several piezoelectric transducers mounted at various distances along the tube are used to trigger the laser and data acquisition electronics. Fig. 2(a) shows a schematic of the experimental setup.

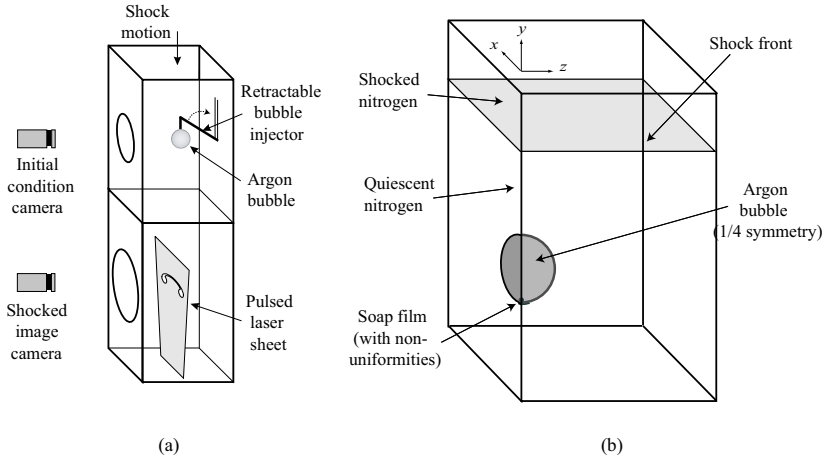

Fig. 2. Schematic setup for shocked bubble experiments using planar laser imaging at WiSTL (a) and for RAPTOR calculations (b).

3 Numerical Simulation

The multi-fluid compressible hydrodynamics code RAPTOR is employed for this purpose. RAPTOR solves the 3-D compressible Euler equations, with an ideal gas law equation of state. The shocked bubble problem is treated here in 3-D because, although the initial condition possesses inherent axisymmetry, previous and current simulations with RAPTOR show that azimuthal variations develop in the vortex rings at late times, due to 3-D vortex bending modes [10]. A shock-capturing scheme and higher-order Godunov solver [11] are used to handle shock propagation properly and suppress spurious oscillations. The calculations are carried out on an Eulerian grid, with adaptive mesh refinement (AMR) applied to achieve high resolution of the fluid interfaces at minimal computational cost [12]. Two levels of AMR are used, with refinement ratios of 4 and 2, giving approximately 130 grid points per bubble radius ($R = 2.5$ cm).

One quadrant of the problem is treated in these calculations, using a 3-D Cartesian coordinate system whose y-axis is coaxial with the shock tube centerline. Symmetry conditions are imposed on all bounding surfaces of the computational domain parallel to the freestream flow, and inflow/outflow on those perpendicular to the flow. The outer bounding surfaces coincide with the position of the side walls of the shock tube, so that the effects of shock wave reflections from the side walls are captured. In the initial condition, one quadrant of a spherical argon volume of diameter $D = 5$ cm is suspended in a quiescent nitrogen atmosphere. This argon bubble is contained within a thin, dense film which separates it from the ambient nitrogen. A planar shock wave with a specified density, velocity, and pressure jump approaches from above.

The finest cell resolution in the AMR mesh (195 μm) is insufficient to resolve the experimental film thickness. Since the film is thus a sub-cell feature, the following two steps are used to model it. First, an appropriately reduced density is assigned to the film material, to ensure that the correct film mass is present in the calculation. Second, the film material is distributed smoothly to represent a spherical surface and constrain the film thickness to the finest cell size in the mesh. Stair-step artifacts are thus avoided by tangentially redistributing film material along the argon-film and film-nitrogen interfaces. As an additional step in modeling the film, excess material is added on the lower extremity of the bubble, on both the inner and the outer surfaces. This excess mass represents tiny interior and exterior droplets (on the order of $D/25$ in size) that form as a result of the technique used to form the bubble film and quickly release it into the shock tube.

4 Results

Experimental and computational times, measured from the time of the initial shock-bubble interaction, are normalized by the quantity $t_c = R/W_t$ where R is the bubble radius and W_t the speed of the planar transmitted shock that would be achieved if the same shock accelerating the bubble struck a planar interface between the same two gases.

For the $M = 3.38$ case, the experimental and computational results for the shocked bubble are compared in Fig. 3. In this case, $t_c \approx 21.7$ μs for an argon bubble initially of radius 2.54 cm. Both the real time t and the nondimensional time τ are noted along with the experimental and computational figures. Experimental images represent light scattered from atomized film material in the bubble midplane; computational images are 2-D plots of the argon volume fraction on the $y - z$ plane. Figs. 3(a) and 3(b) are taken on a single CCD frame in dual exposure mode. Thus, after cropping, the subsequent and previous exposure can be seen in both Figs. 3(a) and 3(b), respectively.

This sequence of experimental and computational flow visualizations shows a similar general trend in the morphology of the shocked bubble. Figs. 3(a,b,e,f) illustrate the initial compression of the bubble to an ellipsoidal shape. Developing vortical structures can be seen in the Figs. 3(b,f) at the sides of the bubble where the baroclinic vorticity deposition is strongest (see Fig. 1). Fig. 3(c,d) shows the resulting primary vortex ring in the downstream end of the bubble which is closely duplicated in the simulation Fig. 3(g,h). In both experiments and simulation, it can be observed that the primary vortex ring is the dominant vortical structure. It entrains most of the bubble gas, rolling it up at the downstream end, subsequently re-expanding the steamwise dimension (height) of the bubble. The computations indicate that the multiple jets and vortex structures visible at later times are due to initial nonuniformities in the bubble film. After passage of the shock, the excess material present in the lower extremity of the bubble film (see Fig. 1(b)) travels vertically across the midplane of the bubble, emerging at late times in the form of a distinct jet and a series of secondary vortex rings at the upper extremity of the bubble as seen in Fig. 3(g,h). These features are also seen in the experiment, though the scales appear much larger, and the vortical structures are less distinct, due to overexposed regions of the images.

In order to study the compression and unstable growth of the bubble, the transverse ("width," W) and axial ("height," H) dimensions of the shocked bubble, excluding the secondary jet, are measured over time and compared to the corresponding values extracted from numerical results for $M = 2.88$ and $M = 3.38$. The data are normalized by the initial bubble diameter D, and plotted *vs.* the nondimensional timescale τ in Fig. 4.

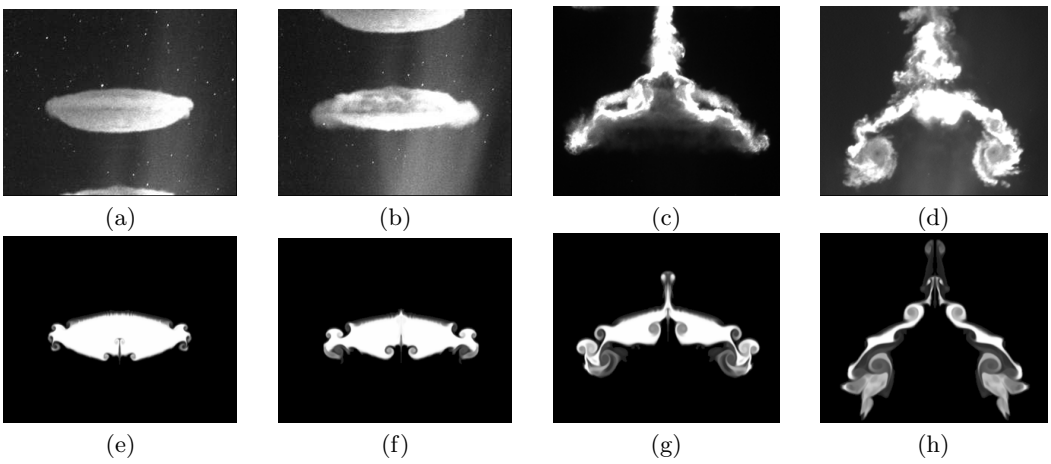

Fig. 3. Experimental images (a,b,c,d) and computational argon volume fraction (e,f,g,h) plotted on grayscale, for $M = 3.38$ shock in nitrogen incident on an argon bubble. Non-domensional times τ are given relative to shock arrival at the top of the bubble. (a) $\tau = 2.0$ ($t \approx 42$ μs), (b) $\tau = 4.0$ ($t \approx 84$ μs), (c) $\tau = 7.1$ ($t \approx 158$ μs), (d) $\tau = 14.3$ ($t \approx 324$ μs), (e) $\tau = 3.0$ ($t \approx 65$ μs), (f) $\tau = 4.6$ ($t \approx 100$ μs), (g) $\tau = 7.9$ ($t \approx 172$ μs), (h) $\tau = 14.7$ ($t \approx 319$ μs).

The transverse growth trends plotted in Fig. 4(a) shows the lateral expansion of the bubble for $\tau < 5$, while the axial growth trends shown in Fig. 4(b) indicate a corresponding compression. Computational and experimental results show good agreement during this phase, for the axial growth trend, though experimental results show higher lateral growth rates. After $\tau \approx 10$, the effect of shock reflections from the shock tube side walls can be seen on the transerse growth plot in Fig. 4(a). In the simulations, this halts the lateral growth, though in the experiment, it dramatically decreases the bubble width. In the axial growth trend shown in Fig. 4(b), the re-expansion effect is much stronger in the experiment than in the simulation, even though the effect of the secondary jet is not included.

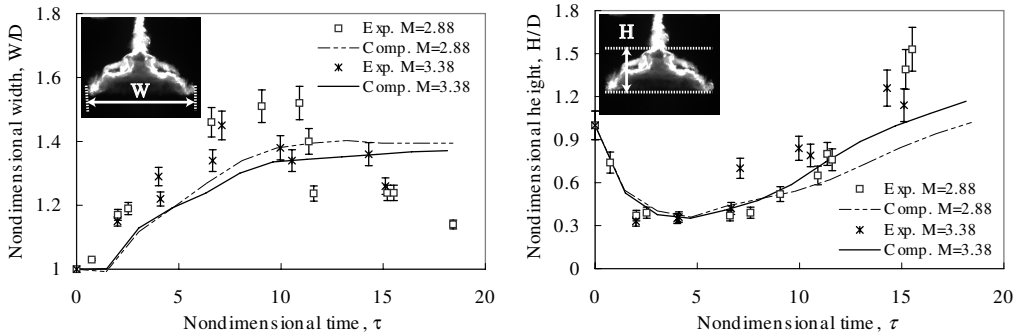

Fig. 4. Nondimensionalized growth trends for shocked bubble, $M = 2.88, 3.38$: (a) transverse dimension, or "width," W; (b) axial dimension, or "height," H.

5 Conclusions

The present work represents a novel experimental approach which takes advantage of planar imaging, higher shock strength than previous experiments, and a flow that is unobstructed by bubble holders or injectors. This approach facilitates the observation of the large characteristic vortex ring that forms in the post-shock flow. Comparison with computational results indicates general agreement in the growth trends for integral length scales.

Simulations show the behavior of the shocked bubble is strongly influenced by the nonuniformities that exist initially in the film material. This study also shows the nondimensional time scale τ provides a useful means of comparing experiments that differ in incident shock strength.

6 Acknowledgements

The authors would like to acknowledge the financial support of the Department of Energy (through grant No. DE-FG03-98DP00207).

References

1. J.D. Kilkenny: 'A review of the ablative stabilization of the Rayleigh-Taylor instability in regimes relevant to inertial confinement fusion', Phys. Plasmas **1**, 5 (1994) pp. 1379–1389
2. B. Jun, T.W. Jones, and M.L. Norman: 'Interaction of Rayleigh-Taylor fingers and circumstellar cloudlets in young supernova remnants', Astrophys. J. **468** (1996) L59-L63
3. Ye. Ye. Meshkov: 'Instability of a shock wave accelerated interface between two gases', NASA Technical Translation F-13,074 (1970)
4. M. Brouillette and B. Sturtevant: 'Experiments on the Richtmyer-Meshkov instability: small scale perturbations on a continuous interface', Phys. Fluids **5** 4 (1993) pp. 916–930
5. R. Bonazza and B. Sturtevant: 'X-ray measurements of growth rates at a gas interface accelerated by shock waves', Phys. Fluids **8** 9 (1996) pp. 2496–2512
6. M.A. Jones and J.W. Jacobs: 'A membraneless experiment for the study of Richtmyer-Meshkov instability of a shock-accelerated gas interface', Phys. Fluids **9**(10) (1997) pp. 3078–3085
7. J.H. Haas and B. Sturtevant: 'Interaction of weak shock waves with cylindrical and spherical gas inhomogeinities', JFM **181** (1987) pp. 41–76
8. G. Layes, G. Jourdan and L. Houas: 'Experimental investigation of the shock wave interaction with a spherical gas inhomogeneity', Phys. Fluids **17** (2005) pp.028103-1:4
9. M.H. Anderson, B.P. Puranik, J.G. Oakley, P.W. Brooks, and R. Bonazza: 'Shock tube investigation of hydrodynamic issues related to inertial confinement fusion', Shock Waves **10** (2000) pp. 377–387
   'The interaction of supernova remnants with interstellar clouds: experiments on the NOVA laser', Astrophys. J. **583** (2003) pp. 245–259
10. S.E. Widnall, D.B. Bliss, and C.Y. Tsai: 'The instability of short waves on a vortex ring', J. Fluid Mech. **66** (1974) p. 35.
11. P. Colella: 'A direct Eulerian MUSCL scheme for gas dynamics', SIAM J. Sci. Stat. Comput. **6** 104 (1985) p. 104.
12. M. Berger and P. Colella: 'Local adaptive mesh refinement for shock hydrodynamics', J. Comput. Phys. **82** (1989) p. 64.